



Space Weather®



RESEARCH ARTICLE

10.1029/2021SW002715

Key Points:

- Ionospheric irregularities are found to be strongest during post-midnight hours than pre-midnight hours in Asian and African-American longitudinal sectors
- Upward propagating gravity waves (GWs) and ionospheric irregularities show three dominant peaks around Asian, African-American, and west Pacific sectors
- GWs are derived from Sounding of the Atmosphere using Broadband Emission Radiometry satellite temperature measurements to assess the relationship between GWs and ionospheric irregularities

Correspondence to:

E. B. Seba, biboephy@gmail.com

Citation:

Seba, E. B., Nigussie, M., Giday, N. M., & Moldwin, M. B. (2021). The relationship between upward propagating atmospheric gravity waves and ionospheric irregularities during solar minimum periods. *Space Weather*, 19, e2021SW002715. https://doi.org/10.1029/2021SW002715

Received 3 JAN 2021 Accepted 10 OCT 2021

© 2021. The Authors.

This is an open access article under the terms of the Creative Commons Attribution-NonCommercial-NoDerivs License, which permits use and distribution in any medium, provided the original work is properly cited, the use is non-commercial and no modifications or adaptations are made.

The Relationship Between Upward Propagating Atmospheric Gravity Waves and Ionospheric Irregularities During Solar Minimum Periods

Ephrem B. Seba¹, Melessew Nigussie², Nigussie M. Giday¹, and Mark B. Moldwin³

¹Space Science and Applications Research Development, Ethiopian Space Science and Technology Institute, Addis Ababa, Ethiopia, ²Physics Department, Washera Geospace and Radar Science Laboratory, Bahir Dar University, Bahir Dar, Ethiopia, ³Climate and Space Sciences and Engineering, University of Michigan, Ann Arbor, MI, USA

Abstract We present a study on the relationship between upward propagating gravity waves and ionospheric irregularities. Gravity waves (GWs) are identified from Thermosphere Ionosphere Mesosphere Energetics and Dynamics (TIMED) satellite temperature measurements and nighttime ionospheric irregularities are observed from the three Swarm satellites. Using these two independent set of measurements, we investigate the relationship between gravity waves and ionospheric irregularities on both equinox and solstice seasons for the years 2018–2019. The results show, post-sunset gravity wave characteristics are important in understanding the variability of global nighttime equatorial plasma density irregularities. We also find out that the pre-midnight and post-midnight characteristics of ionospheric irregularities show global westward shift in the occurrence of ionospheric irregularities. Upward propagating gravity waves also show three dominant peaks longitudinally with the strongest being between American and African longitudinal sectors. Strongest gravity wave amplitudes are associated with strongest plasma irregularities. GW suppression is observed around equatorial regions at stratopause region in our measurements which are commonly observed at polar and higher latitudinal regions in many studies. We also observe that, ionospheric irregularities are strongest when GWs are relatively less suppressed.

Plain Language Summary Atmospheric gravity waves are medium scale waves originating from different altitudes in the lower and middle atmosphere due to topographic sources (airflow around mountains), convective sources and wind shears. This waves are the main agents in transporting energy and momentum from the lower atmosphere to the upper atmospheric (thermospheric/ionospheric) heights thereby dynamically connecting the two regions. Nighttime ionospheric irregularities are plasma density irregularities in the Earth's ionosphere primarily created due to plasma density instability in the nighttime ionosphere. We utilize gravity waves derived from Sounding of the Atmosphere using Broadband Emission Radiometry satellite temperature measurements and plasma irregularities derived from Swarm satellite plasma density measurements to investigate the relationship between vertically upward propagating gravity waves and ionospheric nighttime plasma density irregularities. The results show that post-sunset gravity wave characteristics are important in understanding the variability of global nighttime plasma density irregularities. Strongest gravity wave amplitudes are associated with strongest plasma irregularities. Upward propagating gravity wave suppression (attenuation) on global scales is observed in which plasma irregularities are strongest when gravity waves are relatively less attenuated. Understanding the characteristics of plasma irregularities is very important because of its impact on radio wave communications. These impacts on radio wave communications can degrade ground- and satellitebased communications and navigation systems.

1. Introduction

Coupling process between the lower and upper thermosphere/ionosphere through gravity waves (GWs) has been observed by many studies (Crowley et al., 1987; Djuth et al., 2004; Hocke & Tsuda, 2001; Hocke et al., 1996; Oliver et al., 1997; Porter & Tuan, 1974; Shibata, 1983). These waves originate from different altitudes in the lower and middle atmosphere due to topographic sources (mountain waves), convective sources and wind shears (Fritts & Alexander, 2003). GWs are one of the main agents in transporting energy

SEBA ET AL. 1 of 15



and momentum from the lower atmosphere to the thermospheric/ionospheric heights thereby dynamically connecting the two regions. When upward propagating GWs become unstable, the wave breaks and results in loss of energy (Fritts & Rastogi, 1985; Fritts & Yuan, 1989; Lindzen, 1981). The flux and energy dissipation of GWs increases as they propagate upward and their influences become more pronounced in the mesosphere and lower thermosphere (Fritts & Alexander, 2003). In addition, airglow observation of GWs by Fritts and Vadas (2008), Vadas and Fritts (2009), and Vadas and Nicolls (2009) showed that GWs can penetrate to much higher altitudes under suitable conditions.

GW amplitude increases as it propagates vertically upward due to an exponential decrease in air density and mechanical friction. Moreover, at certain altitudes GW attenuation can result due to radiative cooling effect, which is caused by carbon dioxide and ozone layer. Reddy and Vijayan (1989) and Vijayan and Reddy (1994) theoretically described effective attenuation of vertically propagating GWs at different altitudes in the equatorial region. In general vertically upward propagating GW can be represented as

$$e^{i\left(w_{d}t-k_{x}x-k_{z}z\right)}\tag{1}$$

where

$$\omega_d = \omega - k_x U \tag{2}$$

where k_x and k_z are wavenumbers in the east-west and vertical directions respectively assuming eastward and upward propagations as positive. U and ω are zonal wind speed and angular frequency of the wave respectively and ω_d is the doppler-shifted wave frequency. According to their finding, wave attenuation over short path (Δz) at any altitude is given by $\exp(-k_i\Delta z)$ and the total wave attenuation between altitudes z_1 and z_2 will therefore given by

$$D = \exp\left[-\left(\sum_{z_1}^{z_2} k_i \, \Delta z\right)\right] \tag{3}$$

where $k_{\rm i}$ is the imaginary part of vertical wavenumber appropriately associated with the radiative cooling rate. Therefore, from Equation 3, we can estimate the effective attenuation if we know the dissipation rate caused by radiative cooling at various altitudes. According to Reddy and Vijayan (1989) and references therin, radiative cooling rate is maximum for the altitude range between around 40–60 km, which is around stratopause region. Therefore, from this we can expect vertical GW attenuation due to radiative cooling around stratopause region. That is, vertically propagating GWs in this altitude ranges will be attenuated based on Equation 3. Our measurements also indicate that GWs are attenuated in this altitude range. The effective wave attenuation is governed by the wave growth due to exponential decrease in density, which is represented by $e^{z/2H}$, and the opposite effect by radiative cooling. Therefore the effective attenuation between altitudes z_1 and z_2 is given by

$$D_{\text{eff}} = \exp\left[\sum_{z_1}^{z_2} \left(1/2H(z) - k_i(z)\right) \Delta z\right]$$
(4)

where *H* is the scale height of the atmosphere. So as GWs propagate vertically upward, their amplitude increases as a function of altitude due to exponential decrease in air density, but the waves will be attenuated at altitudes where radiative cooling effect is maximum.

Equatorial ionospheric plasma density irregularities, which are generally known as equatorial spread F, are electron density irregularities observed right after sunset in the equatorial regions. As a result of stronger upward $E \times B$ plasma drift around sunset hours, denser plasma moves to higher altitudes resulting in plasma density instability. The existence of sharp vertical density gradient at F2 bottom side is an important initial condition for the growth of nighttime plasma bubbles. The most widely accepted theory for the generation of nighttime plasma irregularities is the Rayleigh-Taylor instability (RTI) mechanism. The growth rate (γ_g) of generalized Rayleigh-Taylor instability mechanism is defined as (Sekar & Raghavarao, 1987):

$$\gamma_g = \frac{1}{L} \left\{ \frac{g}{\nu_{\text{in}}} + \frac{E_x}{B} + W_x \left(\frac{\nu_{\text{in}}}{\Omega_i} \right) - W_z \right\}$$
 (5)

SEBA ET AL. 2 of 15



where

$$1/L = (1/Ni)(dNi/dz)$$
(6)

where Ni is the electron/ion density of the ionosphere, g is acceleration due to Earth's gravity, $v_{\rm in}$ is ion-neutral collision frequency and L is the scale height of the plasma density at F2 bottomside. $W_{\rm x}$ and $W_{\rm z}$ are the zonal and vertical winds, respectively. $\Omega_{\rm t}$ is the ion gyro frequency.

The role of gravity waves in initiating or seeding nighttime plasma bubbles is investigated in many studies based on observational data and numerical solutions to RTI mechanism (Abdu et al., 2009; Huang & Kelley, 1996; Keskinen et al., 2003; Krall et al., 2013; Tsunoda, 2010; Zalesak et al., 1982). According to Abdu et al. (2009), comparison of observations from radar and digisond measurements with theoretical models indicated seeding of equatorial ionospheric irregularities by gravity waves. They found that perturbation winds caused by GWs can significantly contribute to the polarization electric field thereby controlling the growth rate of irregularities depending on F layer vertical velocity and height, and vertical density gradient at F layer bottom side. They solved the RTI analytically and showed that

$$\delta E_x = S_x / \gamma_g \left(\exp \gamma_g t - 1 \right) \tag{7}$$

where δE_x is zonal polarization electric field and S_x is source function which is proportional to vertical density gradient. S_x is a form of wind perturbation (δW) related to seeding gravity waves. They concluded that gravity wave induced perturbations can be an efficient source for the growth rate of RTI (Abdu et al., 2009). Keskinen et al. (2003) and Zalesak et al. (1982) showed that plasma density perturbations attributed to gravity waves initiate plasma bubbles during the post-sunset hours. It is clear that turbulence inside magnetized plasma is very important as it results in polarization electric fields and perturbations in local electric fields thereby causing fluctuations in upward $E \times B$ plasma drift that triggers ionospheric irregularities. Zonal electric field fluctuations and the associated plasma density fluctuations or initiation of plasma density irregularities are investigated in different studies (Yizengaw & Groves, 2018). This indicates the importance of factors that affect zonal electric field in initiating plasma density irregularity growth rate. In addition to gravity wave initiation of plasma irregularities, the study of gravity wave turbulence in seeding equatorial ionospheric irregularities using a three dimensional ionospheric model indicated that gravity wave associated zonal and vertical winds are found to be most effective in seeding ionospheric irregularities (Wu et al., 2015).

Vertically upward propagating GWs in equatorial region during post-midnight hours can induce an eastward electric field thereby triggering ionospheric irregularities. Post-midnight irregularities ranging from strong to longitudinally broad depletions were measured by Burke et al. (2009). They detected deep plasma depletions at topside altitudes after local midnight as the result of eastward polarization electric fields. Huang et al. (2010) also found that ionospheric irregularities are frequently observed in post-midnight hours and argued that the cause for this is not understood. Interestingly, the electric field in the plasma depletions is significantly enhanced during post-midnight hours according to Huang et al. (2010). Normally ionospheric irregularities are generated around sunset terminator hours. Although the mechanism how ionospheric irregularities form after midnight is not well understood, recent studies are indicating that GWs are potential candidates for the occurrence of the post-midnight ionospheric irregularities. Yizengaw et al. (2013) showed the existence of RTI after midnight hours through physics-based models indicating that one potential source for the generation of eastward electric field during post-midnight hours are gravity waves. A recent work for solar minimum periods by Otsuka (2018) showed that GWs can effectively initiate RTI through electric field perturbations during post-midnight periods resulting in irregularity formations. But the role of day-to-day variability of GWs on the day-to-day variability of ionospheric irregularities requires high resolution simultaneous measurement and assessment of GWs, PRE and ionospheric irregularities. A recent study by Abdu (2019) also suggested that the investigation of the role of GWs as a precursor of equatorial plasma bubbles requires simultaneous assessment primarily of PRE and vertical drift amplitude including other related parameters.

Ionospheric irregularities show daily, seasonal, longitudinal and solar cycle variabilities (Burke et al., 2004; Gentile et al., 2006; Huang & Burke, 2004). But the natural mechanism why irregularities show day-to-day,

SEBA ET AL. 3 of 15



seasonal and longitudinal variabilities are some of the longstanding questions in the study of equatorial ionospheric irregularities (Abdu et al., 2009; Saito & Maruyama, 2007; Yizengaw & Groves, 2018). Moreover, the variability of ionospheric irregularities in ionospheric irregularity seasons (March and September) is not clear. Nigussie et al. (2020) showed that longitudinal variability of $E \times B$ which is the main cause for RTI mechanism, is caused by neutral winds. In this paper we present the longitudinal and vertical characteristics of gravity waves in association with the longitudinal characteristics of ionospheric irregularities using measurements from two independent sources: SABER (Sounding of the Atmosphere using Broadband Emission Radiometry) instrument on board the TIMED satellite measures atmospheric temperature from which gravity waves are estimated and plasma density obtained from the three Swarm satellites. Therefore, this study investigates the characteristics of upward propagating GWs and their impact on the variability of pre-midnight and post-midnight ionospheric irregularities on global scales.

The paper is organized as follows: In Section 2, we provide discussion on the methods of extracting gravity waves from SABER satellite temperature measurements and also methods of ionospheric plasma density irregularity calculations. In Sections 3 and 4, we present the results and discussions respectively, of the study. Finally in Section 5, we summarize the main findings of the study and conclusions.

2. Data Analysis

In this study we used independent measurements of plasma densities (Swarm A, B, and C satellites) from which ionospheric irregularities were derived and temperature profile (SABER/TIMED satellite) to derive GWs. Rate of plasma density index (RODI) sampled for 10 seconds are used as proxy for the existence of irregularities from the three Swarm satellite data. The sampling rate of the Swarm satellite data is 0.5 s. RODI is calculated as follows:

$$ROD = \left(\frac{\Delta Ni}{\Delta t_{sw}}\right)_{\Delta t_{sw} = 0.5s}$$
(8)

and

$$RODI = \sqrt{\langle ROD^2 \rangle + \langle ROD^2 \rangle}$$
 (9)

where the rate of density (ROD) measures change in plasma density (ΔNi) for every successive 0.5 s and RODI is the standard deviation of ROD sampled for 10 s. Based on the orbital speed of the Swarm satellite which is 7.6 km/s (Dunlop & Luhr, 2020), the spatial scale of ionospheric irregularities represented by RODI in our case is between 7.6 and 76 km. This RODI is used as proxy for ionospheric irregularities (Zakharenkova et al., 2016). Gravity waves are calculated using temperature measurements from SABER/TIMED satellite with the same method as described in Liu et al. (2017) and Gong et al. (2019). In this work we used monthly level 2 SABER temperature data to study the equinoctial and solstice GW characteristics from 2018 to 2019 March equinox (February, March and April), September equinox (August, September, and October), December solstice (November, December, and January) and June solstice (May, June, and July). The SABER temperature measurement (T) data are first arranged as longitude versus height ($25^{\circ} \times 1$ km) for the range between ±40° latitudes for both the ascending and descending orbits of the satellite separately. In gravity wave extraction method, different studies used different longitudinal bin size. For instance Yamashita et al. (2013) used the longitudinal bin size as 20° whereas John and Kumar (2013) used 24° longitudinal bin size. In our case we used 25° longitudinal bin size and then we performed least square harmonic fitting with wave numbers 0-7 for each height profile of the temperature (T(z)) and obtained amplitudes and phase angles of a harmonic series $(A^*\cos(kx+\phi))$. The amplitudes and phases are used to construct a new temperature profile (T_o) which is background temperature (John & Kumar, 2013; Liu et al., 2017). The wave numbers 0-7 represent longer background waves like tides and planetary waves (Liu et al., 2017). In this case, the correlation between the observation and the fitted is almost one. The background temperature (T_a) is then subtracted from the measurement (T) to obtain temperature perturbations (T') caused by gravity waves $(T' = T - T_o)$. We then performed wavelet analysis (morlet) on each T'(z). GW reconstruction is made for vertical wavelengths in the range between 4 and 30 km (Liu et al., 2017). Then a new perturbation temperature is reconstructed in this wavelength range. This process is done for both the ascending and

SEBA ET AL. 4 of 15

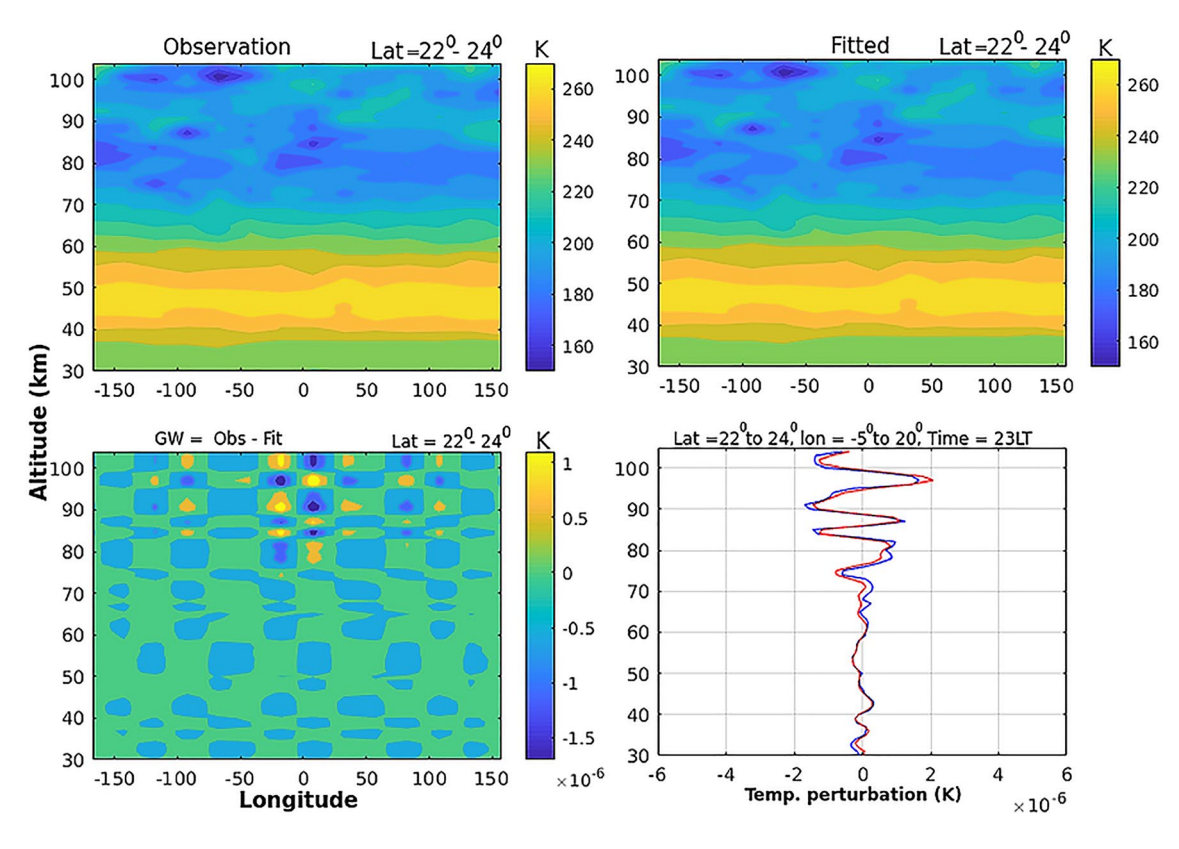


Figure 1. Examples of gravity wave extraction on September, 2017 where (a) temperature observation or measurement (b) harmonic fitting to the measurement (c) temperature perturbations due to gravity wave (GW) calculated as GW = Observation-fit (d) temperature perturbation due to GW at particular latitude, longitude and local time.

descending orbits of the satellite separately and then the final GW is calculated as the difference (ascending-descending orbits) in order to remove the effects of diurnal atmospheric tides (Remsberg et al., 2008). Example on extracting gravity waves can be seen from Figure 1. Logarithmic gravity wave amplitudes are calculated as $10*\log 10$ (T^2) where T is GW temperature perturbation (Yamashita et al., 2013).

3. Results

Global morphology of both ionospheric irregularities and vertical propagation of gravity waves for September equinox 2018 can be seen from Figure 2. It can be seen that there are three dominant upward propagating gravity waves propagating from stratosphere to lower thermosphere (30-105 km) for the time 18-24 LT as seen by the three arrows (Figure 2b). The middle one being in between ≈±50 longitudes and the other two are -50 to -180 and 50-180 longitudes. The gravity wave is strongest in $\approx \pm 50$ than the two other regions. Interestingly the longitudinal characteristics of ionospheric irregularities shows three dominant structures in these mentioned three regions with the ±50 being the strongest (Figures 2a and 2c). In addition, the post-midnight characteristics of both the gravity waves and ionospheric irregularities show similar trends. There are three dominant upward propagating gravity waves that nearly matches with the three dominant ionospheric irregularity structures which are in the west Pacific, Atlantic and the Asian sectors. Moreover, the post-midnight period measured strongest ionospheric irregularities and GWs. Three dominant GW peaks have been observed in different ground-based and satellite-based measurements in different studies around Asian, African-Atlantic, and the American regions (Alexander et al., 2008; Ern et al., 2018; Hertzog et al., 2002; Tsuda et al., 2000; Zhang et al., 2012). An interesting characteristic of equatorial and mid-latitudinal ionospheric irregularities are observed before midnight and after midnight in the above mentioned longitudinal sectors. In-between the American - African sector, the ionospheric irregularities originated from African sector during the 18-24 LT hours and later it shifted to Atlantic sector following

SEBA ET AL. 5 of 15

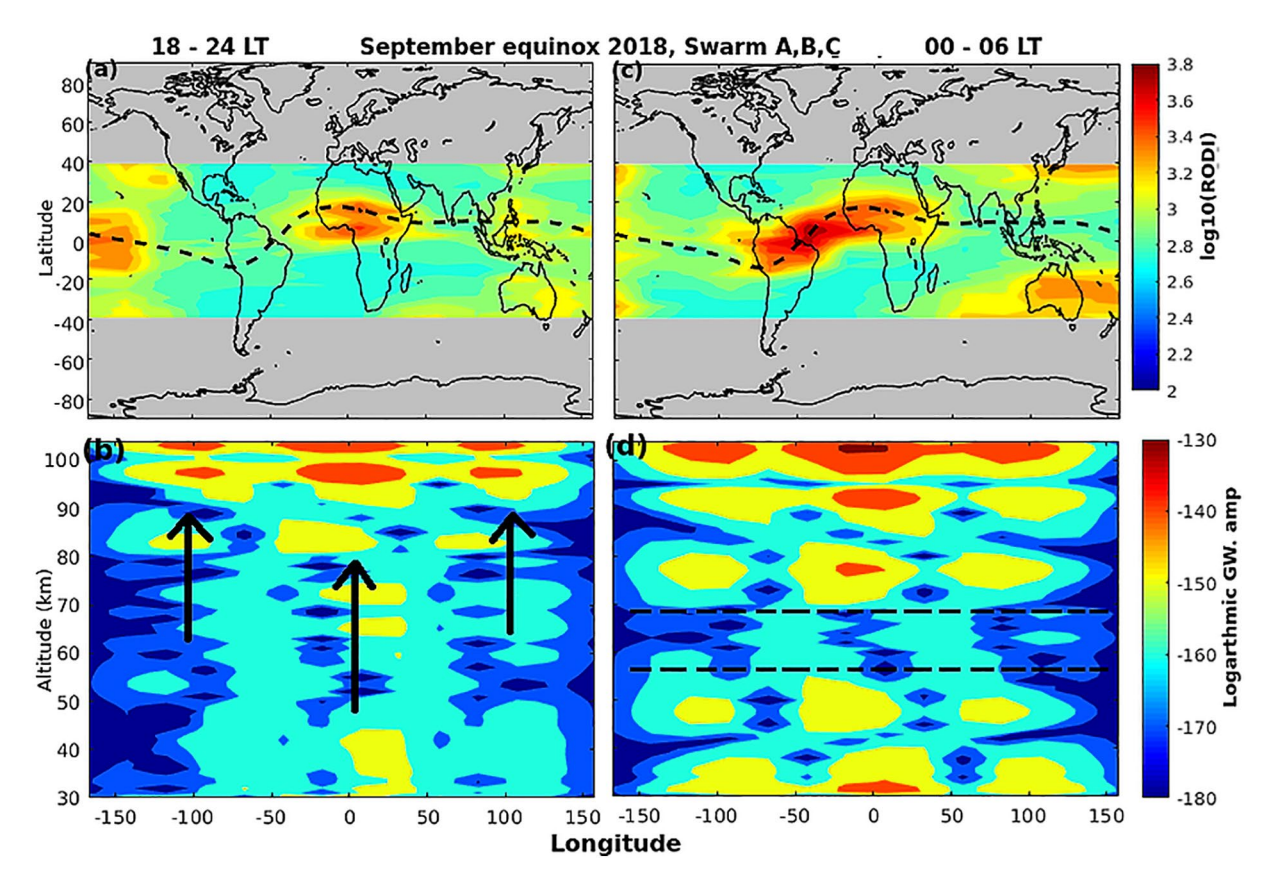


Figure 2. The upper plots (a and c) are logarithmic Rate of plasma density index (RODI) plots. The bottom plots (b and d) are logarithmic gravity wave (GW) amplitudes for 18–24 LT and 00–06 LT respectively for September equinox 2018.

the dip magnetic equatorial line during 00-06 LT as indicated by the arrow (Figure 2c). The west Pacific sector equatorial and mid-latitudinal ionospheric irregularities showed stronger magnitude during 18-24 LT and significantly decreased after midnight. The Asian sector showed relatively weaker magnitudes during pre-midnight hours and increased its magnitude after midnight (Figures 2a and 2c) indicating westward shift in the occurrence of ionospheric irregularities in these regions. The westward shift is the result of shift in local time. That is the pre-sunset sector at a particular sector later changes to post-sunset/pre-midnight sector and this same sector later changes to post-midnight sector indicating westward shift in the local night time periods. Since irregularities become stronger during the post-midnight sector, which is shifting toward the west, the occurrence of irregularity also shifts toward the west. In addition, some deviations between irregularities in the west pacific and Asian sectors with the GWs underneath may also caused by this westward shifting. Irregularity in the American-African sector is better correlated with the GWs underneath although there is westward shift in irregularity occurrence in this sector. The GW in the American-African sector is wider in range and stronger so that the shift in irregularity in this sector also approximately lies in this wider and stronger GW regions. Since the GWs in the west Pacific and Asian sectors are relatively weaker in strength and narrower in range as compared to the American-African longitude sector so that shift in irregularity occurrence in this sectors results in some deviations between ionospheric irregularity locations and GWs underneath. Besides the relationship between global trend of GWs and ionospheric irregularities, our results also confirmed an interesting vertical characteristics of GWs. That is GW attenuation around stratopause altitudes is clearly observed as indicated by dashed lines (Figure 2d). This is observed in both pre-midnight and post-midnight GW vertical propagation in our results which will be discussed below.

In March equinox for 2018, clear shift in ionospheric irregularity occurrence from around west African sector to Atlantic sector similar to that of September equinox season before and after midnight hours is observed (Figures 3a and 3c). The GWs showed three longitudinally distinct upward propagating characteristics in which the American-African sector is the strongest for both pre-midnight and post-midnight

SEBA ET AL. 6 of 15

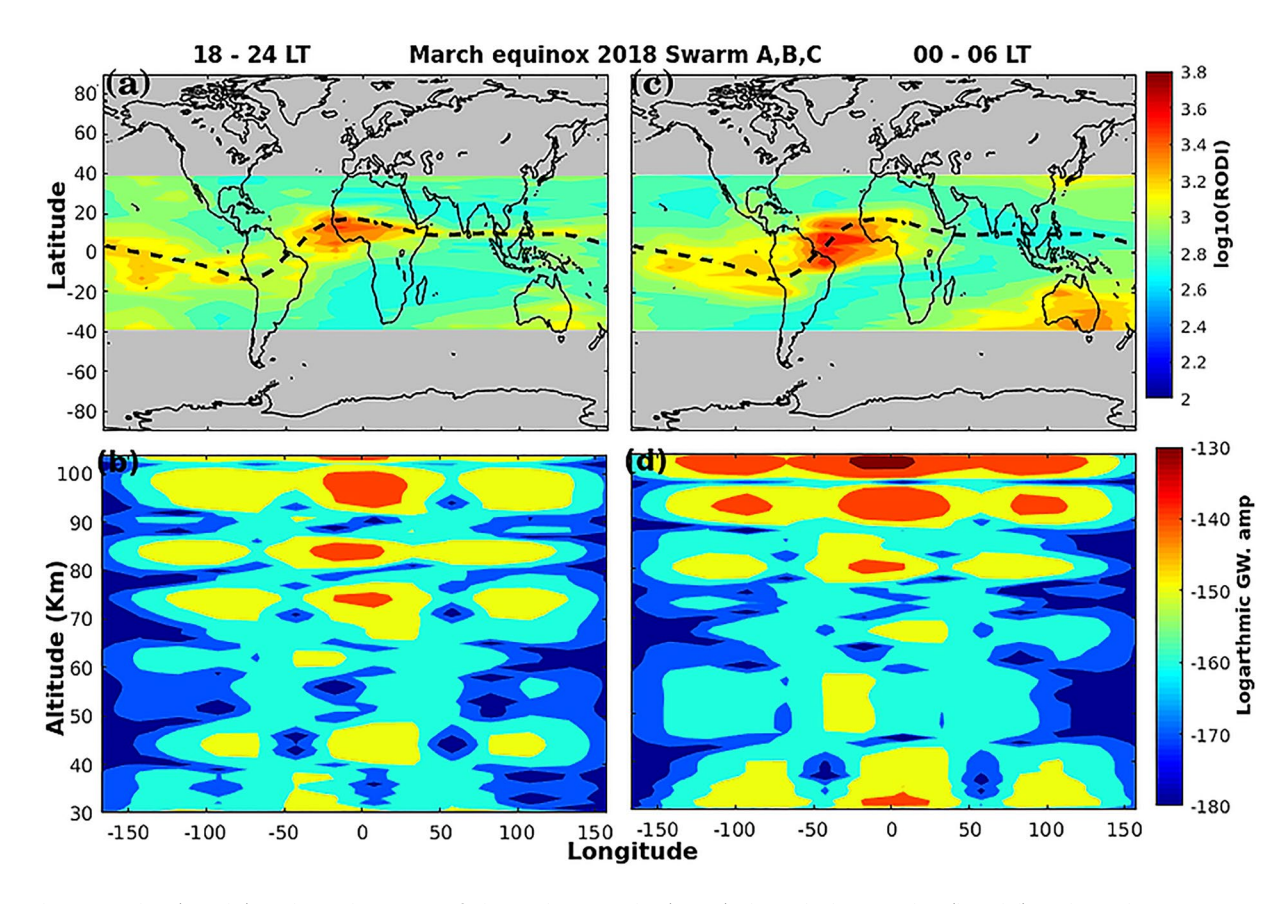


Figure 3. The upper plots (a and c) are logarithmic Rate of plasma density index (RODI) plots. The bottom plots (b and d) are logarithmic gravity wave (GW) amplitudes for 18–24 LT and 00–06 LT respectively for March equinox 2018.

hours (Figures 3b and 3d). The equatorial ionospheric irregularities in the American-African sector during post-midnight hours is found to be stronger while the GW is also stronger in this time period, showing that stronger ionospheric irregularity magnitudes measured where there are stronger GWs. Here again, attenuation and enhancement of GWs around stratopause region is observed for both pre-midnight and post-midnight hours (Figures 3b and 3d). More interestingly, GW suppression is relatively stronger in the west Pacific and Asian sectors while the African-American GW suppression is relatively less affected (Figures 3b and 3d).

Figure 4 shows the December solstice season for 2018 and shows the ionospheric irregularities in $\approx \pm 50$ again started around west African sector and then showed clear shift to Atlantic and American sectors after midnight in addition to intensification in its magnitude. Similarly, the mid-latitude ionospheric irregularities in the west Pacific sector showed stronger magnitude during pre-midnight hours and weaker magnitudes after midnight. But the reverse is true for the characteristics of mid-latitudinal ionospheric irregularities in the Asian sector in that, the magnitude of mid-latitude ionospheric irregularity is weaker in the pre-midnight hours than post-midnight hours. This again indicates a westward shift in the occurrence of ionospheric irregularities. Moreover, stratospheric GW attenuation is also observed in this season before and after midnight hours with the African-American sector being relatively less affected similar to the September and March equinox seasons discussed above. As we have discussed for September and March equinox as well as December solstice, GWs are relatively less suppressed in African-American sectors where there is the strongest ionospheric irregularity activity during all seasons than the other longitudinal sectors (Figures 2–4).

The GW and ionospheric irregularity trends for June solstice season in Figure 5 similarly show three dominant peaks in the three longitude sectors. Although the characteristics of ionospheric irregularities in the west Pacific sector and in the Asian sector show westward shift in the occurrence of ionospheric

SEBA ET AL. 7 of 15

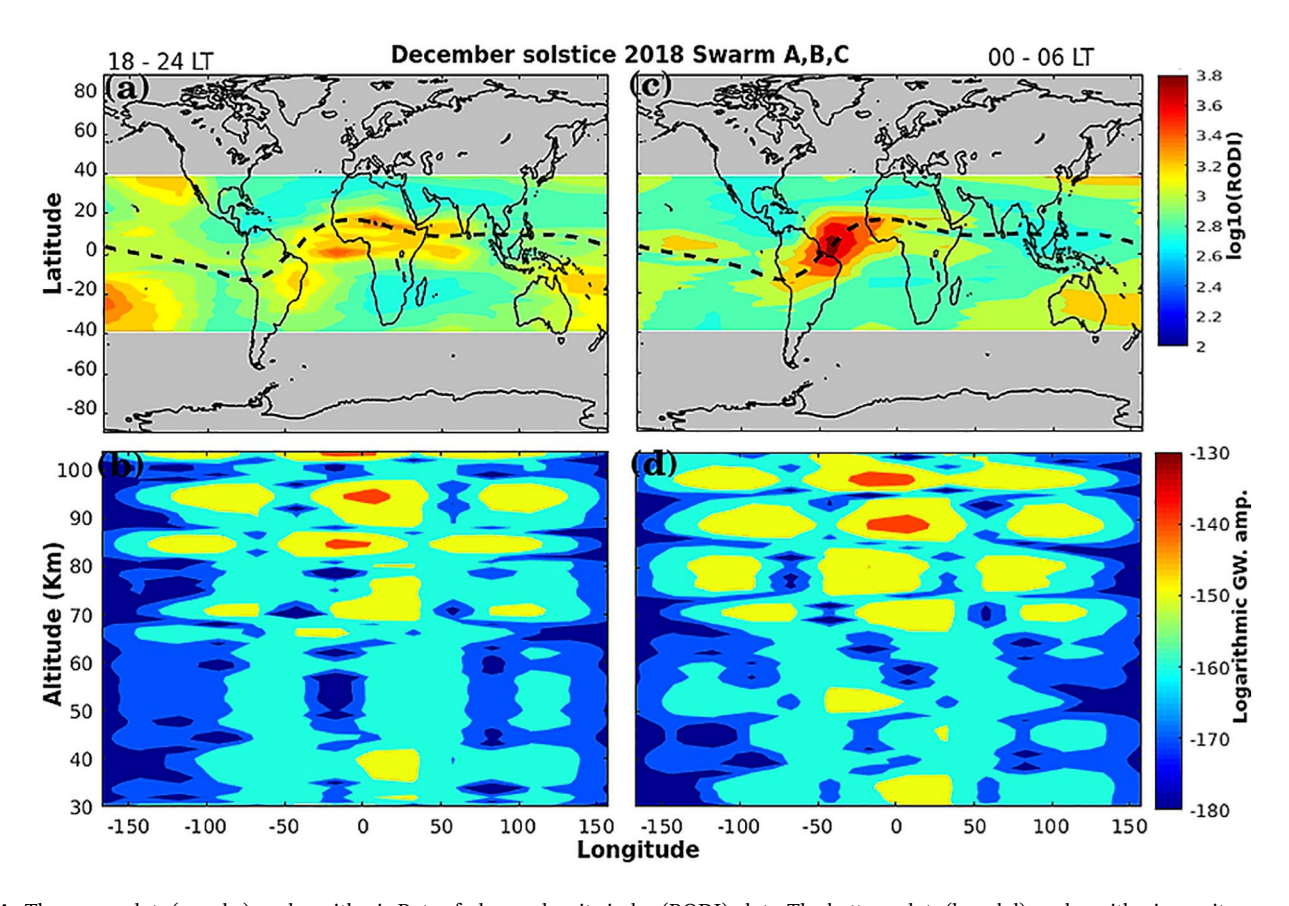


Figure 4. The upper plots (a and c) are logarithmic Rate of plasma density index (RODI) plots. The bottom plots (b and d) are logarithmic gravity wave (GW) amplitudes for 18–24 LT and 00–06 LT respectively for December solstice 2018.

irregularities, the African - American ionospheric irregularity characteristics does not show noticeable shift as can be seen from Figures 5a and 5c. Instead the ionospheric irregularities in the African sector intensified in magnitude after midnight. The GW in June solstice showed stronger upward propagation during pre-midnight hours but significantly decreased after midnight. Although stronger GWs are observed for pre-midnight hours in June solstice, GW is highly suppressed after midnight (Figures 5b and 5d).

In September equinox for 2019 (Figure 6), both the GW and ionospheric irregularities showed three dominant peaks in the three longitude sectors as discussed earlier. The ionospheric irregularities during pre-midnight hours initiated with smaller magnitudes in the African sector and later intensified in magnitude and shifted to the west African - American sector during post-midnight hours (Figures 6a and 6c). Moreover, both equatorial and mid-latitudinal ionospheric irregularities in the west Pacific sector are stronger before midnight and decreased its magnitude after midnight. But the reverse is true for the characteristics of mid-latitudinal ionospheric irregularities in the Asian sector. This again shows the global westward shift in the occurrence of ionospheric irregularities. GWs show three dominant structures before and after midnight hours with the post-midnight GWs being stronger where the ionospheric irregularities are also stronger.

In March equinox for 2019, the occurrence of ionospheric irregularity shifted from African sector during pre-midnight hours to the African – American sector after midnight hours (Figures 7a and 7c). The Asian sector as discussed earlier becomes stronger after midnight while the west Pacific sector diminishes after midnight. When we see the GWs, it is stronger during post-midnight hours where the ionospheric irregularity is stronger. In March equinox 2019, GW suppression is clearly observed as indicated by circles for both pre-midnight and post-midnight hours (Figures 7b and 7d). In this case also, ionospheric irregularity is stronger where the GW is relatively less suppressed in the African - American sector. December solstice measured strongest ionospheric irregularity activity in the African - American sector where there is stronger GW activity after midnight hours in our observation in 2019 (Figures 8a–8d). Moreover, equatorial

SEBA ET AL. 8 of 15

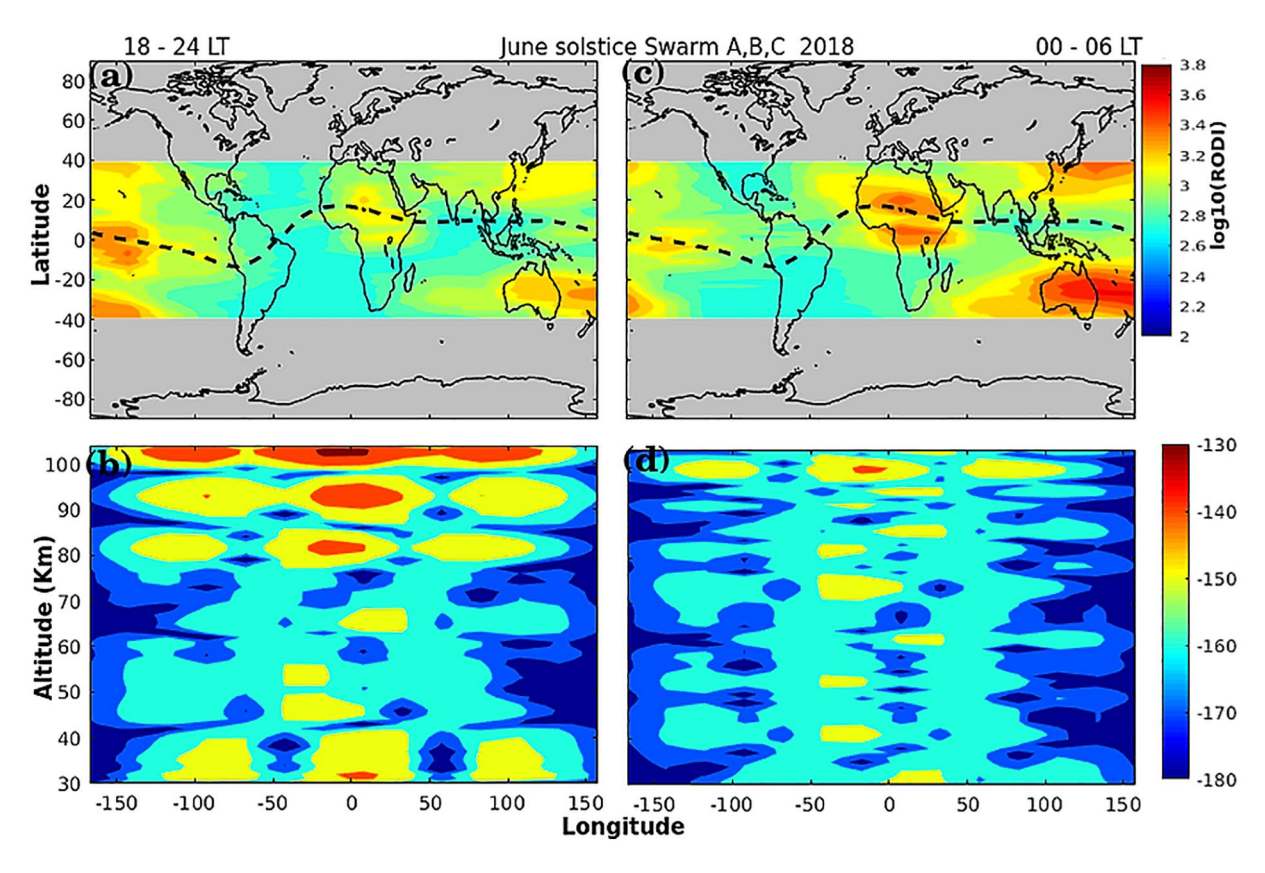


Figure 5. The upper plots (a and c) are logarithmic Rate of plasma density index (RODI) plots. The bottom plots (b and d) are logarithmic gravity wave (GW) amplitudes for 18–24 LT and 00–06 LT respectively for June solstice 2018.

and mid-latitude ionospheric irregularity activity in the west Pacific and Asian sectors show similar trends to that of September and March equinox seasons as discussed earlier. The GWs also show similar global trend to that of the equinox seasons. In June solstice, although there are dominant equatorial and mid-latitude ionospheric irregularity activity observed in the three longitude sectors as observed in other seasons, ionospheric irregularities in the African - American sector did not show noticeable shift in ionospheric irregularity occurrence after midnight except an increase in magnitude (Figures 9a and 9c). But equatorial and mid-latitudinal ionospheric irregularities in the west Pacific and Asian sectors showed similar trends before and after midnight to that of other seasons. Although the GW shows similar trend to the other seasons, stronger GWs mainly originated from around mesospheric altitudes (60–70 km) for both before and after midnight periods (Figures 9b and 9d). Large scale plasma depletions observed at mid-latitudes around Asian and west Pacific sectors are predominantly in solstice seasons (Figures 2–9) and June solstice had the strongest mid-latitude ionospheric irregularities in our measurements.

4. Discussions

Ionospheric irregularities are known to be stronger during equinox seasons due to the alignment of Sun terminator with Earth's magnetic field so that the electric field and magnetic field orientation results in maximum ExB thereby creating RTI. Although $E \times B$ during solstice season is not as strong as it is during equinox season, the December solstice measured strongest ionospheric irregularity activity in the African — American sector where there is stronger GW activity after midnight hours in our observation in 2019 (Figures 8a–8d). Moreover, ionospheric irregularity activity during December solstice in the west Pacific and Asian sectors show similar trends to that of the two equinox seasons. In addition to that, the GW vertical propagations also show similar global trend to that of the equinox seasons. Furthermore, the occurrence of ionospheric irregularities show westward shift mostly for December solstice and the two equinox seasons. It means that irregularity forming hours after sunset occur ahead of time in African sector than Atlantic

SEBA ET AL. 9 of 15

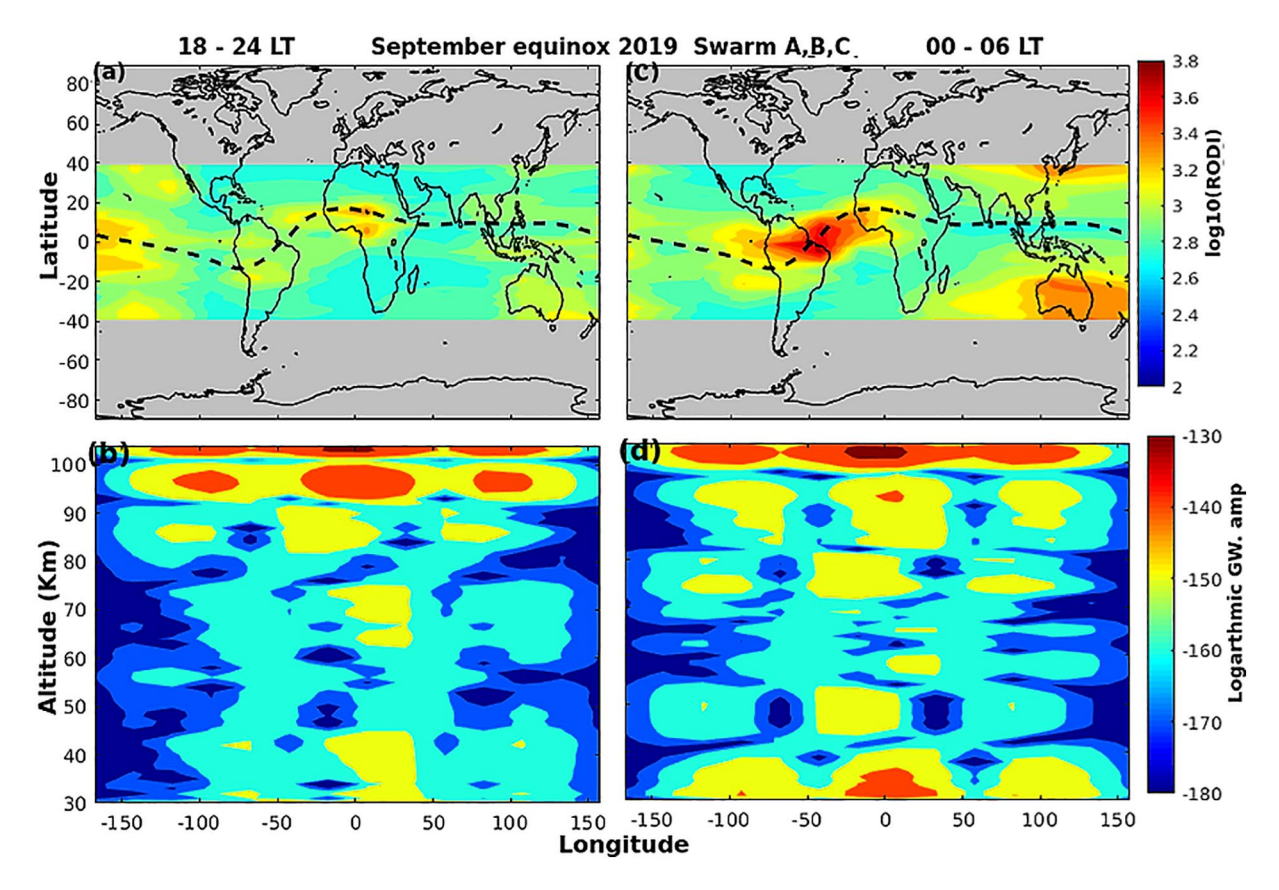


Figure 6. The upper plots (a and c) are logarithmic Rate of plasma density index (RODI) plots. The bottom plots (b and d) are logarithmic gravity wave (GW) amplitudes for 18–24 LT and 00–06 LT respectively for September equinox 2019.

sector and the American sector lags the two sectors. On the other hand, many studies showed westward drift of ionospheric irregularities with respect to the background plasma based on satellite and ground-based measurements (Ajith et al., 2015; Hysell et al., 1990; Kil et al., 2014; McClure et al., 1977; Ossakow, 1979; Yokoyama et al., 2011).

Post-midnight GWs can be a likely candidate to the observation of strong ionospheric irregularities during post-midnight hours in December solstice and the two equinox seasons. Our result on strong post-midnight irregularities is consistent with interesting results found in Dao et al. (2011). Their results indicate that ionospheric irregularities are stronger during post-midnight hours than pre-midnight hours throughout the year for solar minimum years. Olwendo et al. (2019) also confirmed that post-midnight irregularities are stronger than pre-midnight irregularities using RODI measurements from Swarm satellite data and ground-based scintillation measuring receivers.

In our results, June solstice had the strongest mid-latitude ionospheric irregularities in the west Pacific and Asian-Australian sectors. Extensive study of mid-latitude ionospheric irregularities based on ionosonde measurements in Bowman (1990) showed that the occurrence rate of ionospheric irregularity over Australian sector is high during June solstice season for solar minimum periods. According to Bowman (1990) breaking of GWs play central role for the occurrence of ionospheric irregularity structure at mid-latitudes. The GW strength in June solstice showed different characteristics than the other seasons for the two years in that it is stronger during pre-midnight hours than post-midnight hours. Moreover, the characteristics of ionospheric irregularities and GW strength during June solstice are not well correlated as compared to the other seasons for the two years. Since ionospheric irregularity formation is governed by different factors like vertical plasma gradient, elevation of equatorial F-region, background thermospheric winds, plasma density magnitude, vertical plasma drift and GWs, considering the role of the combination of all the major factors is very important. An interesting work by Ajith et al. (2016) indicated that the vertical density gradient and

SEBA ET AL. 10 of 15

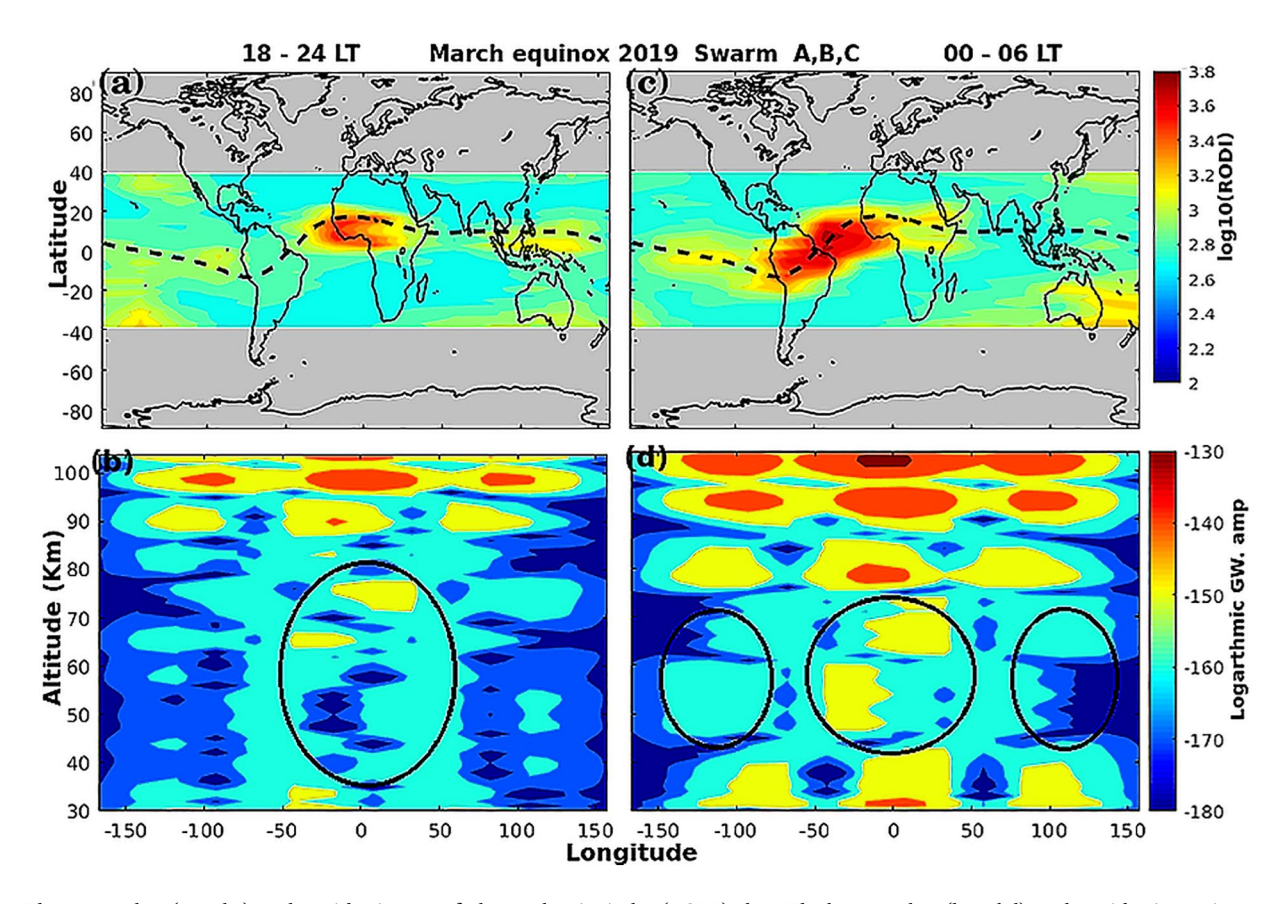


Figure 7. The upper plots (a and c) are logarithmic Rate of plasma density index (RODI) plots. The bottom plots (b and d) are logarithmic gravity wave (GW) amplitudes for 18–24 LT and 00–06 LT respectively for March equinox 2019.

Rayleigh-Taylor growth rate during June solstice maximized around midnight between 22:00 and 03:00 LT. Moreover, Maruyama (1990) also indicated that $E \times B$ drift instability results in ionospheric irregularity formation at mid-latitudes. Perkin's instability can well explain the occurrence of plasma depletions in the mid-latitude regions (Perkins, 1973). Since Perkin's instability growth rate is small ($10^{-4}S^{-1}$), an initial seeding mechanism like gravity waves is required according to Yokoyama and Stolle (2017).

The other interesting result is stratospheric attenuation of GWs as they propagate vertically upward. It is a confirmation of GW suppression observed in many studies from different ground and satellite-based measurements for both orographic and non-orographic GWs (France et al., 2012; Siskind et al., 2007; Yamashita et al., 2010, 2013). Usually stratopause exists in altitude range between \approx 50 and 60 km and an increase in stratopause altitude is termed as elevated stratopause (Manney et al., 2008). Blocking and suppression of GWs in stratosphere is observed in Siskind et al. (2007) and Yamashita et al. (2013).

5. Conclusions

In this study we investigated the vertical propagation and longitudinal characteristics of equatorial and low latitudinal gravity waves (±40 latitudes) in association with the longitudinal characteristics of ionospheric irregularities for equinox and solstice seasons between 2018 and 2019. Based on the results of this study, the following conclusions can be drawn.

 In our results, vertical propagation of GWs show suppression around equatorial regions at the stratopause region. On the other hand, GW suppression is commonly observed at polar and higher latitudinal regions in many studies (France et al., 2012; Siskind et al., 2007; Yamashita et al., 2010, 2013). Stratospheric GWs are relatively less suppressed in the African - American sector where ionospheric irregularity is

SEBA ET AL. 11 of 15

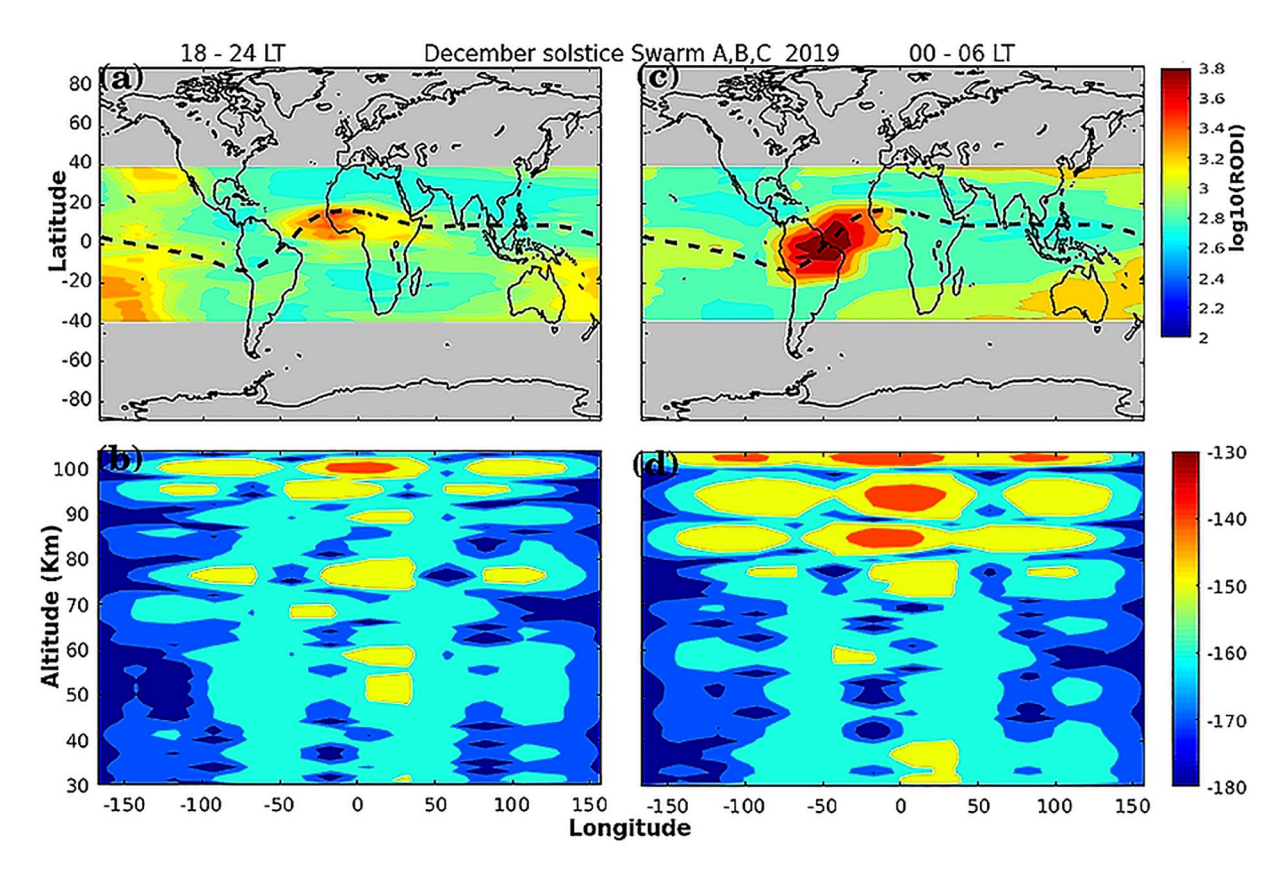


Figure 8. The upper plots (a and c) are logarithmic Rate of plasma density index (RODI) plots. The bottom plots (b and d) are logarithmic gravity wave (GW) amplitudes for 18–24 LT and 00–06 LT respectively for December solstice 2018.

strongest. Gravity wave amplitude strength can be one of the most important factors in understanding the variability and strength of ionospheric irregularities.

- 2. Dominant ionospheric irregularities occur in three regions globally. In between ≈±50, −50 to −180 and 50 to 180 longitudes. Characteristics of ionospheric irregularities in the west Pacific and the Asian longitude sectors showed similar characteristics in all the seasons (equinox and solstice). In the west Pacific sectors ionospheric irregularities are found to be stronger during pre-midnight hours and decreases its magnitude after midnight. The reverse is true for the Asian sectors in that ionospheric irregularities are weaker in pre-midnight hours and stronger after midnight. This may indicate westward shift in the occurrence of ionospheric irregularities between west Pacific region to the Asian sectors. The westward shift is related to shift in local hours. That is, the pre-sunset period at a particular sector changes to post-sunset/pre-midnight period in a later time and this same sector later changes to post-midnight sector indicating westward shift in the local night time periods. Since irregularities become stronger during the post-midnight sector, which is shifting toward the west, the occurrence of irregularities also shifts toward the west.
- Both equatorial and mid-latitude ionospheric irregularities are observed in west Pacific sector, while
 mostly mid-latitude irregularities are observed over Asian-Australian sector. Mid-latitude ionospheric
 irregularities mainly occur during solstice seasons predominantly during June solstice.
- 4. The ionospheric irregularities in the American African sector showed interesting characteristics in that the ionospheric irregularities originated in the central African sector during pre-midnight hours and later intensified in magnitude and shifted to the American Atlantic sectors following the dip magnetic equatorial line for all seasons except June solstice. This indicates westward shift in the occurrence of ionospheric irregularities between African and American longitude sectors. It means that irregularity forming hours after sunset occur ahead of time in African sector than Atlantic sector and the American sector lags the two sectors.

SEBA ET AL. 12 of 15

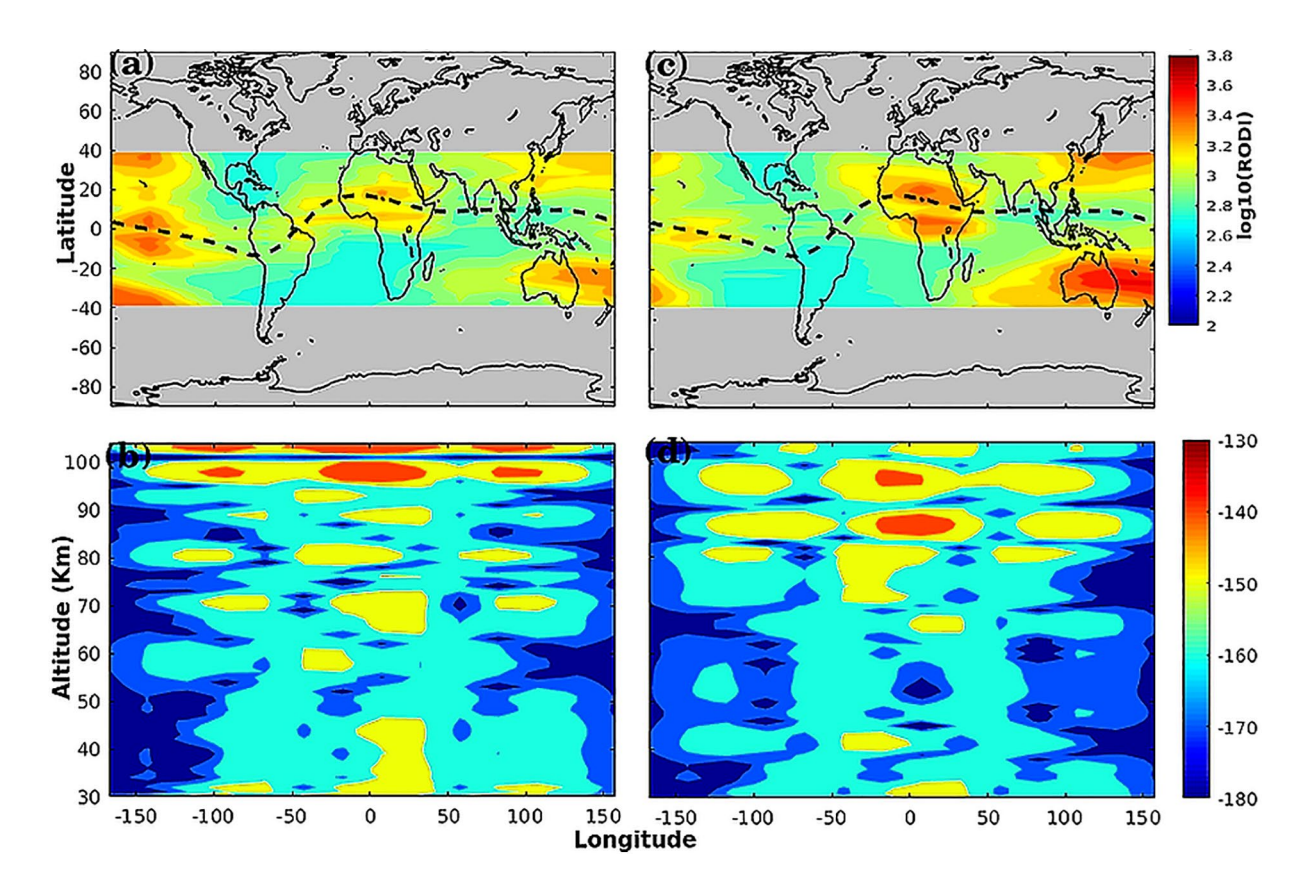


Figure 9. The upper plots (a and c) are logarithmic Rate of plasma density index (RODI) plots. The bottom plots (b and d) are logarithmic gravity wave (GW) amplitudes for 18–24 LT and 00–06 LT respectively for June solstice 2019.

- 5. The vertical propagation and longitudinal characteristics of GWs also showed three dominant peaks in the above mentioned longitudinal sectors. One of the puzzles in the study of ionospheric irregularity characteristics is the strongest ionospheric irregularity magnitudes observed in American African sectors. Our results indicated that strongest GWs and ionospheric irregularities are observed in the American-African sector. Furthermore, Blanc et al. (2014) also showed with 10 years of observations that GWs are very strong in the West African region where there are intense thunderstorms Our results are consistent with this observation in that GW is strongest around west African- Atlantic regions for all seasons.
- 6. The GW strength in June solstice showed different characteristics than the other seasons in that it is stronger during pre-midnight hours than post-midnight hours. Moreover, the characteristics of ionospheric irregularities and GW strength during June solstice are not well correlated for pre-midnight and post-midnight hours as compared to the other seasons for the two years

Data Availability Statement

SABER/TIMED satellite data are available at http://saber.gats-usa.net/overview.php. The Swarm satellite data are available at https://www.gfz-potsdam.de/en/section/geomagnetism/infrastructure/swarm/data-products/.

Acknowledgments

The authors greatly acknowledge SABER/TIMED and Swarm data services for freely providing the satellite data. The authors are also grateful for the Reviewers and the Editor for their constructive comments. M. B. Moldwin was partially supported by NSF Grant AGS 1450512.

References

Abdu, M. A. (2019). Day-to-day and short-term variabilities in the equatorial plasma bubble/spread F irregularity seeding and development. *Progress in Earth and Planetary Science*, 6(1), 1–22. https://doi.org/10.1186/s40645-019-0258-1

Abdu, M. A., Kherani, E. A., Batista, I. S., De Paula, E. R., Fritts, D. C., Sobral, J. H. A., et al. (2009). Gravity wave initiation of equatorial spread {F}/plasma bubble irregularities based on observational data from the spread {F}Ex campaign. *Annales Geophysicae*, 27(7), 2607–2622. https://doi.org/10.5194/angeo-27-2607-2009

SEBA ET AL. 13 of 15



- Ajith, K. K., Ram, S. T., Yamamoto, M., Yokoyama, T., Gowtam, V. S., Otsuka, Y., et al. (2015). Explicit characteristics of evolutionary-type plasma bubbles observed from equatorial atmosphere radar during the low to moderate solar activity years 2010–2012. *Journal of Geophysical Research: Space Physics*, 120(2), 1371–1382. https://doi.org/10.1002/2014ja020878
- Ajith, K. K., Tulasi Ram, S., Yamamoto, M., Otsuka, Y., & Niranjan, K. (2016). On the fresh development of equatorial plasma bubbles around the midnight hours of June solstice. *Journal of Geophysical Research: Space Physics*, 121(9), 9051–9062. https://doi.org/10.1002/2016ja023024
- Alexander, S. P., Tsuda, T., Kawatani, Y., & Takahashi, M. (2008). Global distribution of atmospheric waves in the equatorial upper troposphere and lower stratosphere: COSMIC observations of wave mean flow interactions. *Journal of Geophysical Research*, 113(D24), D24115. https://doi.org/10.1029/2008jd010039
- Blanc, E., Farges, T., Le Pichon, A., & Heinrich, P. (2014). Ten year observations of gravity waves from thunderstorms in western Africa. Journal of Geophysical Research: Atmospheres, 119(11), 6409–6418. https://doi.org/10.1002/2013jd020499
- Bowman, G. G. (1990). A review of some recent work on mid-latitude spread-F occurrence as detected by ionosondes. *Journal of Geomagnetism and Geoelectricity*, 42(2), 109–138. https://doi.org/10.5636/jgg.42.109
- Burke, W. J., de La Beaujardière, O., Gentile, L. C., Hunton, D. E., Pfaff, R. F., Roddy, P. A., et al. (2009). C/NOFS observations of plasma density and electric field irregularities at post-midnight local times. *Geophysical Research Letters*, 36(18), L00C09. https://doi.org/10.1029/2009gl038879
- Burke, W. J., Gentile, L. C., Huang, C. Y., Valladares, C. E., & Su, S. Y. (2004). Longitudinal variability of equatorial plasma bubbles observed by DMSP and ROCSAT-1. *Journal of Geophysical Research*, 109(A12), A12301. https://doi.org/10.1029/2004ja010583
- Crowley, G., Jones, T. B., & Dudeney, J. R. (1987). Comparison of short period TID morphologies in Antarctica during geomagnetically quiet and active intervals. *Journal of Atmospheric and Terrestrial Physics*, 49(11–12), 1155–1162. https://doi.org/10.1016/0021-9169(87)90098-5
- Dao, E., Kelley, M. C., Roddy, P., Retterer, J., Ballenthin, J. O., de La Beaujardiere, O., & Su, Y.-J. (2011). Longitudinal and seasonal dependence of nighttime equatorial plasma density irregularities during solar minimum detected on the C/NOFS satellite. *Geophysical Research Letters*, 38(10), L10104. https://doi.org/10.1029/2011gl047046
- Djuth, F. T., Sulzer, M. P., Gonzales, S. A., Mathews, J. D., Elder, J. H., & Walterscheid, R. L. (2004). A continuum of gravity waves in the Arecibo thermosphere? Geophysical Research Letters, 31(16), L16801. https://doi.org/10.1029/2003gl019376
- Dunlop, M. W., & Lühr, H. (2020). Ionospheric multi-spacecraft analysis tools: Approaches for deriving ionospheric parameters (pp. 288). Springer Nature.
- Ern, M., Trinh, Q. T., Preusse, P., Gille, J. C., Mlynczak, M. G., Russell, J. M., III, & Riese, M. (2018). GRACILE: A comprehensive climatology of atmospheric gravity wave parameters based on satellite limb soundings. *Earth System Science Data*, 10(2), 857–892. https://doi.org/10.5194/essd-10-857-2018
- France, J. L., Reay, H. J., King, M. D., Voisin, D., Jacobi, H. W., Domine, F., et al. (2012). Hydroxyl radical and NOx production rates, black carbon concentrations and light-absorbing impurities in snow from field measurements of light penetration and nadir reflectivity of onshore and offshore coastal Alaskan snow. *Journal of Geophysical Research*, 117(D14), D00R12. https://doi.org/10.1029/2011jd016639
- Fritts, D. C., & Alexander, M. J. (2003). Gravity wave dynamics and effects in the middle atmosphere. *Reviews of Geophysics*, 41(1). https://doi.org/10.1029/2001rg000106
- Fritts, D. C., & Rastogi, P. K. (1985). Convective and dynamical instabilities due to gravity wave motions in the lower and middle atmosphere: Theory and observations. *Radio Science*, 20(6), 1247–1277. https://doi.org/10.1029/rs020i006p01247
- Fritts, D. C., & Vadas, S. L. (2008). Gravity wave penetration into the thermosphere: Sensitivity to solar cycle variations and mean winds. Annales Geophysicae, 26(12), 3841–3861. https://doi.org/10.5194/angeo-26-3841-2008
- Fritts, D. C., & Yuan, L. (1989). Stability analysis of inertio—Gravity wave structure in the middle atmosphere. *Journal of the Atmospheric Sciences*, 46(12), 1738–1745. https://doi.org/10.1175/1520-0469(1989)046<1738:saoiws>2.0.co;2
- Gentile, L. C., Burke, W. J., & Rich, F. J. (2006). A climatology of equatorial plasma bubbles from DMSP 1989–2004. *Radio Science*, 41(5). https://doi.org/10.1029/2005rs003340
- Gong, S., Yang, G., Xu, J., Liu, X., & Li, Q. (2019). Gravity wave propagation from the stratosphere into the mesosphere studied with lidar, meteor radar, and TIMED/SABER. Atmosphere, 10(2), 81. https://doi.org/10.3390/atmos10020081
- Hertzog, A., Vial, F., Mechoso, C. R., Basdevant, C., Cocquerez, P., Dubourg, V., & Nouel, F. (2002). Planetary and gravity wave activity in the equatorial lower stratosphere as seen by ultra-long duration balloons. *Advances in Space Research*, 30(5), 1381–1386. https://doi.org/10.1016/s0273-1177(02)00555-0
- Hocke, K., & Schlegel, K. (1996). A review of atmospheric gravity waves and travelling ionospheric disturbances: 1982–1995. *Annales Geophysicae*, 14(9), 917–940. https://doi.org/10.1007/s005850050357
- Hocke, K., & Tsuda, T. (2001). Gravity waves and ionospheric irregularities over tropical convection zones observed by GPS/MET radio occultation. *Geophysical Research Letters*, 28(14), 2815–2818. https://doi.org/10.1029/2001gl013076
- Huang, C.-S., de La Beaujardiere, O., Pfaff, R. F., Retterer, J. M., Roddy, P. A., Hunton, D. E., et al. (2010). Zonal drift of plasma particles inside equatorial plasma bubbles and its relation to the zonal drift of the bubble structure. *Journal of Geophysical Research*, 115(A7), A07316. https://doi.org/10.1029/2010ja015324
- Huang, C.-S., & Kelley, M. C. (1996). Nonlinear evolution of equatorial spread F: 1. On the role of plasma instabilities and spatial resonance associated with gravity wave seeding. *Journal of Geophysical Research*, 101(A1), 283–292. https://doi.org/10.1029/95ja02211
- Huang, C. Y., & Burke, W. J. (2004). Transient sheets of field-aligned current observed by DMSP during the main phase of a magnetic superstorm. *Journal of Geophysical Research*, 109(A6), 18. https://doi.org/10.1029/2003ja010067
- Hysell, D. L., Kelley, M. C., Swartz, W. E., & Woodman, R. F. (1990). Seeding and layering of equatorial spread F by gravity waves. *Journal of Geophysical Research*, 95(A10), 17253–17260. https://doi.org/10.1029/ja095ia10p17253
- John, S. R., & Kumar, K. K. (2013). A discussion on the methods of extracting gravity wave perturbations from space-based measurements. Geophysical Research Letters, 40(10), 2406–2410. https://doi.org/10.1002/grl.50451
- Keskinen, M. J., Ossakow, S. L., & Fejer, B. G. (2003). Three-dimensional nonlinear evolution of equatorial ionospheric spread-F bubbles. Geophysical Research Letters, 30(16), 1855. https://doi.org/10.1029/2003gl017418
- Kil, H., Lee, W. K., Kwak, Y.-S., Zhang, Y., Paxton, L. J., & Milla, M. (2014). The zonal motion of equatorial plasma bubbles relative to the background ionosphere. *Journal of Geophysical Research: Space Physics*, 119(7), 5943–5950. https://doi.org/10.1002/2014ja019963
- Krall, J., Huba, J. D., Joyce, G., & Hei, M. (2013). Simulation of the seeding of equatorial spread F by circular gravity waves. *Geophysical Research Letters*, 40(1), 1–5. https://doi.org/10.1029/2012gl054022
- Lindzen, R. S. (1981). Turbulence and stress owing to gravity wave and tidal breakdown. *Journal of Geophysical Research*, 86(C10), 9707–9714. https://doi.org/10.1029/jc086ic10p09707

SEBA ET AL. 14 of 15



- Liu, X., Yue, J., Xu, J., Garcia, R. R., Russell, J. M., III, Mlynczak, M., et al. (2017). Variations of global gravity waves derived from 14 years of SABER temperature observations. *Journal of Geophysical Research: Atmospheres*, 122(12), 6231–6249. https://doi.org/10.1002/2017jd026604
- Manney, G. L., Krüger, K., Pawson, S., Minschwaner, K., Schwartz, M. J., Daffer, W. H., et al. (2008). The evolution of the stratopause during the 2006 major warming: Satellite data and assimilated meteorological analyses. *Journal of Geophysical Research*, 113(D11), D11115. https://doi.org/10.1029/2007jd009097
- Maruyama, T. (1990). $E \times B$ instability in the F-region at low-to midlatitudes. *Planetary and Space Science*, 38(2), 273–285. https://doi.org/10.1016/0032-0633(90)90092-5
- McClure, J. P., Hanson, W. B., & Hoffman, J. H. (1977). Plasma bubbles and irregularities in the equatorial ionosphere. *Journal of Geophysical Research*, 82(19), 2650–2656. https://doi.org/10.1029/ja082i019p02650
- Nigussie, M., Moldwin, M. B., Radicella, S., Yizengaw, E., Zou, S., & Nava, B. (2020). The effect of F-layer zonal neutral wind on the monthly and longitudinal variability of equatorial ionosphere irregularity and drift velocity. *Journal of Geophysical Research: Space Physics*, 125(6), e2019JA027671.
- Oliver, W. L., Otsuka, Y., Sato, M., Takami, T., & Fukao, S. (1997). A climatology of F region gravity wave propagation over the middle and upper atmosphere radar. *Journal of Geophysical Research*, 102(A7), 14499–14512. https://doi.org/10.1029/97ja00491
- Olwendo, J., Cilliers, P. J., & Ming, O. (2019). Comparison of ground-based ionospheric scintillation observations with in situ electron density variations as measured by the swarm satellites. *Radio Science*, 54(10), 852–866. https://doi.org/10.1029/2018rs006734
- Ossakow, S. L. (1979). Ionospheric irregularities. Reviews of Geophysics, 17(4), 521-533. https://doi.org/10.1029/rg017i004p00521
- Otsuka, Y. (2018). Review of the generation mechanisms of post-midnight irregularities in the equatorial and low-latitude ionosphere. *Progress in Earth and Planetary Science*, 5(1), 1–13. https://doi.org/10.1186/s40645-018-0212-7
- Perkins, F. (1973). Spread F and ionospheric currents. Journal of Geophysical Research, 78(1), 218–226. https://doi.org/10.1029/ja078i001p00218
- Porter, H. S., & Tuan, T. F. (1974). On the behavior of the F-layer under the influence of gravity waves. *Journal of Atmospheric and Terrestrial Physics*, 36(1), 135–157. https://doi.org/10.1016/0021-9169(74)90072-5
- Reddy, C. A., & Vijayan, L. (1989). Reflection and attenuation of equatorial waves in the stratosphere and mesosphere. *Quarterly Journal of the Royal Meteorological Society*, 115(490), 1273–1299. https://doi.org/10.1002/qj.49711549006
- Remsberg, E. E., Marshall, B. T., Garcia-Comas, M., Krueger, D., Lingenfelser, G. S., Martin-Torres, J., et al. (2008). Assessment of the quality of the version 1.07 temperature-versus-pressure profiles of the middle atmosphere from TIMED/SABER. *Journal of Geophysical Research*, 113(D17), D17101. https://doi.org/10.1029/2008jd010013
- Saito, S., & Maruyama, T. (2007). Large-scale longitudinal variation in ionospheric height and equatorial spread F occurrences observed by ionosondes. *Geophysical Research Letters*, 34(16), L16109. https://doi.org/10.1029/2007gl030618
- Sekar, R., & Raghavarao, R. (1987). Role of vertical winds on the Rayleigh-Taylor mode instabilities of the night-time equatorial ionosphere. *Journal of Atmospheric and Terrestrial Physics*, 49(10), 981–985. https://doi.org/10.1016/0021-9169(87)90104-8
- Shibata, T. (1983). A numerical calculation of the ionospheric response to atmospheric gravity waves in the F-region. *Journal of Atmospheric and Solar-Terrestrial Physics*, 45, 797–809. https://doi.org/10.1016/s0021-9169(83)80019-1
- Siskind, D. E., Eckermann, S. D., Coy, L., McCormack, J. P., & Randall, C. E. (2007). On recent interannual variability of the Arctic winter mesosphere: Implications for tracer descent. *Geophysical Research Letters*, 34(9), L09806. https://doi.org/10.1029/2007gl029293
- Tsuda, T., Nishida, M., Rocken, C., & Ware, R. H. (2000). A global morphology of gravity wave activity in the stratosphere revealed by the GPS occultation data (GPS/MET). *Journal of Geophysical Research*, 105(D6), 7257–7273. https://doi.org/10.1029/1999jd901005
- Tsunoda, R. T. (2010). On seeding equatorial spread F: Circular gravity waves. Geophysical Research Letters, 37(10), L10104. https://doi.org/10.1029/2010gl043422
- Vadas, S. L., & Fritts, D. C. (2009). Reconstruction of the gravity wave field excited by convective plumes via ray tracing in real space. Annales Geophysicae, 27, 147–177. https://doi.org/10.5194/angeo-27-147-2009
- Vadas, S. L., & Nicolls, M. J. (2009). Temporal evolution of neutral, thermospheric winds and plasma response using PFISR measurements of gravity waves. Journal of Atmospheric and Solar-Terrestrial Physics, 71(6–7), 744–770. https://doi.org/10.1016/j.jastp.2009.01.011
- Vijayan, L., & Reddy, C. A. (1994). Radiative damping of equatorial waves in the middle atmosphere. Quarterly Journal of the Royal Meteorological Society, 120(519), 1323–1343. https://doi.org/10.1002/qj.49712051910
- Wu, T.-W., Huba, J. D., Krall, J., Fritts, D. C., & Laughman, B. (2015). Seeding equatorial spread F with turbulent gravity waves: Phasing effects. *Geophysical Research Letters*, 42(1), 15–21. https://doi.org/10.1002/2014gl062348
- Yamashita, C., England, S. L., Immel, T. J., & Chang, L. C. (2013). Gravity wave variations during elevated stratopause events using SABER observations. *Journal of Geophysical Research: Atmospheres*, 118(11), 5287–5303. https://doi.org/10.1002/jgrd.50474
- Yamashita, C., Liu, H.-L., & Chu, X. (2010). Gravity wave variations during the 2009 stratospheric sudden warming as revealed by ECM-WF-T799 and observations. Geophysical Research Letters, 37(22), L22806. https://doi.org/10.1029/2010gl045437
- Yizengaw, E., & Groves, K. M. (2018). Longitudinal and seasonal variability of equatorial ionospheric irregularities and electrodynamics. Space Weather, 16(8), 946–968. https://doi.org/10.1029/2018sw001980
- Yizengaw, E., Retterer, J., Pacheco, E. E., Roddy, P., Groves, K., Caton, R., & Baki, P. (2013). Postmidnight bubbles and scintillations in the quiet-time June solstice. Geophysical Research Letters, 40(21), 5592–5597. https://doi.org/10.1002/2013gl058307
- Yokoyama, T., Pfaff, R. F., Roddy, P. A., Yamamoto, M., & Otsuka, Y. (2011). On postmidnight low-latitude ionospheric irregularities during solar minimum: 2. C/NOFS observations and comparisons with the equatorial atmosphere radar. *Journal of Geophysical Research*, 116(A11), A11326. https://doi.org/10.1029/2011ia016798
- Yokoyama, T., & Stolle, C. (2017). Low and midlatitude ionospheric plasma density irregularities and their effects on geomagnetic field. Space Science Reviews, 206(1-4), 495–519. https://doi.org/10.1007/s11214-016-0295-7
- Zakharenkova, I., Astafyeva, E., & Cherniak, I. (2016). GPS and in situ Swarm observations of the equatorial plasma density irregularities in the topside ionosphere. Earth Planets and Space, 68(1), 1–11. https://doi.org/10.1186/s40623-016-0490-5
- Zalesak, S. T., Ossakow, S. L., & Chaturvedi, P. K. (1982). Nonlinear equatorial spread F: The effect of neutral winds and background Pedersen conductivity. *Journal of Geophysical Research*, 87(A1), 151–166. https://doi.org/10.1029/ja087ia01p00151
- Zhang, Y., Xiong, J., Liu, L., & Wan, W. (2012). A global morphology of gravity wave activity in the stratosphere revealed by the 8-year SABER/TIMED data. *Journal of Geophysical Research*, 117(D21), D21101. https://doi.org/10.1029/2012jd017676

SEBA ET AL. 15 of 15